This is a repository copy of *Microstructural development and mechanical properties of drop tube atomized Al-2.85 wt% Fe*.

White Rose Research Online URL for this paper:
https://eprints.whiterose.ac.uk/174621/

Version: Accepted Version

Article:

Microstructural Development and Mechanical Properties of Drop Tube Atomized Al-2.85wt% Fe

Mehmet R. Abul, Robert F. Cochrane & Andrew M. Mullis

School of Chemical & Process Engineering, University of Leeds,

Leeds LS2 9JT, UK

Abstract

Al-2.85 wt% Fe alloy has been subjected to nonequilibrium containerless solidification using a 6.5 m drop tube. Spherical samples were collected and sieved into 7 sizes fractions ranging from 850 μm to 53 μm, with the estimated cooling rates being 150 to 11000 K s^{-1} respectively. XRD analysis was employed on all droplet size fractions for identification and evolution of the phases, showing that Al, Al_6Fe and $Al_{13}Fe_4$ were formed for all sizes while Al_5Fe_2 was observed only in droplets ≤ 150 μm in diameter. Microstructural evaluation was conducted by using SEM and optical microscopy, showing that droplet larger than 300 μm in diameter exhibited distinct morphologies; microcellular, dendritic α-Al with interdendritic $Al_{13}Fe_4$ eutectic and an Al-Al_6Fe eutectic region. With increasing cooling rate, the Al-Al_6Fe region disappeares. EDX analysis reveals that increasing the cooling rate increased the dissolved Fe content in α-Al from 0.37 wt% Fe to 1.105 wt% Fe, and correspondingly the eutectic fraction decreased from 49.7 vol.% to 26.7 vol.%. Measurement of the lamellar spacing allowed the eutectic growth velocity and interfacial undercooling to be calculated, wherein the Al-rich boundary of the eutectic coupled zone could be reconstructed. This shows a coupled zone skewed significantly towards the intermetallic side of the eutectic. In order to understand the effect of nonequilibrium the solidification on the mechanical properties microhardness of the droplets was measured. The microhardness has risen from 55.3 $HV_{0.01}$ to 66.5 $HV_{0.01}$ for ≥ 850 μm and ≤ 75 μm droplets respectively.

Keywords: Al-Fe alloys, containerless solidification, microstructure, TEM, microhardness

1. Introduction

Fe is present in most secondary Al as an impurity element [1]. The presence of Fe has significant detrimental effects on mechanical properties, corrosion resistance, formability and surface finish of Al alloys by forming intermetallics such as needle like $Al_{13}Fe_4$ [2]. Although $Al_{13}Fe_4$ (also sometimes denoted as Al_3Fe) is the only stable intermetallic phase up to 40 wt% Fe, nonequilibrium solidification processes can promote the formation of a number of thermodynamically metastable intermetallics, which can either improve the mechanical properties, especially, high temperature strength, elastic moduli and thermal stability of iron bearing aluminium alloys [3] or, as a minimum, have a less deleterious effect on the mechanical properties than is the case with $Al_{13}Fe_4$.

These metastable intermetallic phases include the orthorhombic Al_6Fe and Al_5Fe_2 phases [4], together with a range of others intermetallics including Al_mFe (m=4.0 to 4.4), Al_xFe (x=5.0 to 5.5) and Al_9Fe_2 [3]. The formation of these phases, and therefore which phase may be selected,

depends upon the thermal and solidification conditions, as well as Fe concentration of the alloy [5,6]. Of the metastable intermetallics, the transition between stable $Al_{13}Fe_4$ and metastable Al_6Fe appears to be the easiest to facilitate. According to the metastable phase diagram proposed by Murray [7], the Al-$Al_{13}Fe_4$ eutectic composition of 1.7 wt% Fe moves to 2.8 wt% Fe in the Al-Al_6Fe eutectic, although the eutectic temperature is not much changed, being 655 °C for the Al-$Al_{13}Fe_4$ eutectic compared with 648 °C for the Al-Al_6Fe eutectic. However, only very small departures from equilibrium are required to mediate this transition, with Al-Al_6Fe being the dominant eutectic in Bridgman growth experiments at velocities > 0.1 mm s^{-1} and the $Al_{13}Fe_4$ intermetallic disappearing completely for growth velocities above 1-10 mm s^{-1}, depending upon the Fe-concentration of the base alloy [8,9]. This transition corresponds to an interface temperature for the eutectic close to that of the equilibrium eutectic temperature for the growth of the Al-Al_6Fe eutectic. In addition, decagonal quasicrystalline and amorphous phases have been reported via melt spinning and powder milling [4,10]. While quasicrystalline phases can be observed in dilute systems (2.5 at%Fe), amorphization requires higher Fe content as high as 10 at.% Fe [4,11].

Rapid solidification (RS) techniques provide significant microstructural and constitutional changes [10,12,13] in many alloys. Some of the unique properties achieved by RS techniques consist of solid solubility extension, grain size refinement, formation of metastable phases and in some cases formation of amorphous and quasicrystalline phases, with many of these effects improving the mechanical properties of alloys, especially lightweight metals [10,14]. Consequently, there has been considerable interest in exploring whether RS processing of contaminated and mixed alloy scrap Al, particularly via powder metallurgical techniques, can provide a cost effective route to upcycle such scrap without the need for refining the scrap prior to processing[15].

Rapid solidification can be achieved by different techniques including, but not limited to: drop tube processing, electromagnetic levitation, melt spinning and glass fluxing. The drop tube technique is a containerless solidification process which combines deep undercooling and high cooling rate under free-fall conditions, wherein buoyancy driven convection may be much reduced. Such containerless processing eliminates possible heterogeneous nucleation sites from mold/container walls, while the use of high vacuum or inert gas atmospheres within such equipment avoids oxidation, which also reduces the density of favourable sites for heterogeneous nucleation [16–18]. Moreover, drop tube processing provides a good analogue for commercial powder production techniques, such as high pressure gas atomisation (HPGA), and we might reasonably expect that microstructures observed in drop tube studies will be replicated in commercial HPGA powders of similar composition.

Al-Fe alloys have been of interest to many researchers due to various structures with extraordinary physical and mechanical properties [16,19]. The solid solubility of Fe in Al is very low (0.05 at.%) [20]. There are numerous studies on the extension of the solid solubility of Fe in Al via different rapid solidification techniques [4,6,11,20]. In the majority of these, as might be expected, the degree of supersaturation increased with both the Fe-content of the liquid and the level of departure from equilibrium (generally either higher cooling rate or deeper undercooling), with the published extensions ranging between 2 to 10 at.%. However, in one

seemingly anomalous study, Nayak *et al.* [4], using melt spinning on Al-Fe alloys containing between 2.5 to 20 at.% Fe, found that the solid solubility of Fe decreased with increasing Fe content. Perhaps even more surprisingly they found that increasing the linear wheel speed from 20 to 40 m s^{-1}, thus increasing the cooling rate, also decreased the solid solubility of Fe.

Chen *et al.* [3] studied the microstructural evolution of impulse atomized, hypoeutectic Al-0.61 wt% Fe and hypereutectic Al-1.90wt% Fe droplets, with diameters of 355µm and corresponding cooling rates of 95 K s^{-1} and 170 K s^{-1} respectively. They reported that in both samples the primary phase to form was α-Al with a dendritic morphology, rather than an intermetallic [3], a fact they attributed to the shift in the eutectic point under rapid solidification. Al$_m$Fe was found to be the only intermetallic in the hypoeutectic droplet, while in the hypereutectic, and hence faster cooled, alloy Al$_{13}$Fe$_4$ and small amounts of Al$_6$Fe were detected using neutron diffraction and TEM, in addition to Al$_m$Fe. They also reported that the dendritic growth direction for both samples was <111> rather than <100>, <100> being the expected growth direction for fcc metals with a low entropy of fusion [3].

Drop tube studies on the Al-Fe system date back to 1988. Since then, limited researches have been made. In a study by Cochrane *et al.* [21] based on drop tube processed Al-8wt% Fe, 250-120 µm droplets processed in helium showed that primary faceted Al$_{13}$Fe$_4$ and a rod like eutectic between α-Al and Al$_6$Fe formed at lower undercooling, ΔT. Increasing ΔT resulted in the formation of the α-Al + Al$_6$Fe eutectic only. Moreover, increasing the cooling rate, and thus ΔT, changed the morphology of the powders from a fine cellular structure to cellular-dendritic. However, the cooling rate of the droplets in this experiment was not estimated. The minimum undercooling below the liquidus temperature to achieve primary Al, primary Al$_6$Fe and partitionless solidification were estimated as 140 K, 225 K and 290 K, respectively [21]. Similar cellular-dendritic microstructures were also observed by Sharma *et al.* in drop-tube solidified Al-3.6wt% Fe droplets with a diameter of 500 µm produced in a helium atmosphere [22]. Sharma *et al.* found that the primary phase was α-Al with an estimated the undercooling for this alloy of 450 K below the Al$_{13}$Fe$_4$ liquidus, or 375 K below the metastable extension of Al liquidus.

The purpose of this investigation is to characterize rapidly solidified drop tube processed Al-2.85 wt% Fe samples as a function of cooling rate. For this purpose, XRD, optical microscopy, Scanning Electron Microscopy and Transmission Electron Microscopy techniques were employed. The microhardness values of the samples were measured in order to understand the effect of the cooling rate on the mechanical properties.

2. Experimental Procedure

The Al-2.85 wt% Fe alloy was prepared using high purity Al (>99.999 wt%) and high purity (99.9 wt%) fine iron wires. These were melted together in a high vacuum furnace, with the melt being held for 30 minutes at a temperature of 1150 °C before being slowly cooled to room temperature. In order to ensure complete dissolution of the iron, the alloy was sectioned and mounted in resin. The mounted sample was then investigated using XRD, optical microscopy and SEM. After such examination, and making sure that Fe is completely dissolved in Al, the prepared alloy was placed in an alumina crucible which has three laser drilled holes of 300 µm diameter in the base. The alumina crucible was then mounted in a graphite susceptor and sealed

to the top of the drop-tube. Two alumina heat shields were placed around the susceptor, which was induction heated using a 3 kW RF generator.

The drop tube was evacuated to a pressure of 10^{-2} mbar and backfilled with dry, oxygen free, nitrogen gas to a pressure of 500 mbar. This process was repeated 3 times in order to flush any residual oxygen from the drop-tube. The final evacuation was done using a turbomolecular pump to a pressure of 2.7×10^{-5} mbar and the drop-tube was again filled to 400 mbar with dry, oxygen free, nitrogen gas. An R-type thermocouple was inserted into the crucible, just below the level of the melt, to measure the temperature of the sample. Once molten, the melt was ejected by pressurizing the alumina crucible with 4 bar nitrogen gas.

The resulting spherical samples were collected from the bottom of the drop-tube after cooling and sieved in to 7 different size fractions, namely: 850-500 µm, 500-300 µm, 300-212 µm, 212-150 µm, 150 -106 µm, 106-75 µm and 75-53 µm.

The sieved samples were investigated by XRD using a Philips X'Pert Diffractometer with Cu K_{α} radiation and a step size of 0.033° between 2θ values of 20° to 80° at room temperature. Following XRD analysis, the samples were hot mounted in resin. The mounted samples were ground using 800, 1200 and 2000 grit SiC papers progressively. The ground samples were then polished using 6 µm, 3 µm and 1 µm diamond pastes. The final polishing was made using 0.05 µm colloidal silica on a semiautomatic polisher for 1.5 minutes to obtain a scratch free surface finish. Between each grinding and polishing stage, samples were washed using dilute detergent, running water and methanol and then dried with hot air. The samples were checked under optical microscope after each stage. The polished samples were etched for optical microscopy using Keller's Reagent (1% HF, 1.5 % HCl, 2.5% HNO_3 and 95% water).

The microstructures of the samples were analysed using an Olympus BX51 optical microscope, Hitachi Su8230 SEM and Carl Zeiss EVO MA 15 SEM with built-in energy dispersive X-ray analyser (EDS). For SEM analysis, the samples were carbon coated. SEM images were used for additional quantification of the microstructure. A Transmission Electron Microscope (TEM) sample was cut using Focused Ion Beam (FIB) connected to FEI nova 200 NanoLab FEGSEM. The sample was later investigated using FEI Titan3 Themis 300 TEM.

The image processing software 'Image J' was used for the measurement of the volume fraction of the phases and the inter-lamellar spacing from the SEM and optical microscope images. The fraction of eutectic was measured by converting the area of interest in the RGB images to grey scale and using the 'threshold' function in the software. Eutectic spacing and secondary dendrite arm spacing were also measured by using the software. Lines with a length, l, were drawn perpendicular to the lamellar eutectic and the number of lamellar eutectics, c, were count. The lamellar eutectic spacing, λ, were, then, determined by the following equation:

$$\lambda = \frac{l}{c} \qquad (1)$$

With the same procedure being used to measure the Secondary Dendrite Arm Spacing (SDAS).

Microhardness measurements were conducted using a Tukon^{TM} 1202 Wilson Hardness (Vickers) using 10g load at room temperature, with such measurements being made on the

mounted and colloidal silica polished samples. For each sample, at least 10 measurements were made.

3. Results

3.1 Cooling Rate

The cooling rate of the droplets in free-fall down the drop tube cannot be measured. However, the cooling rate of such droplets can be calculated using the heat balance of the solidifying droplets and can be expressed as [23,24]

$$\frac{dT}{dt} \left[C_p^l (1 - f) + C_p^s f \right] + L \frac{df}{dt} = \frac{6}{d \, \rho_l} \left[\varepsilon \, \sigma_{SB} \, (T^4 - T_R^4) + (h_m (T - T_R)) \right] \tag{2}$$

where d is the droplet diameter, C_p^l is the specific heat of the melt, C_p^s is the specific heat of the solid, f is the solid fraction, L latent heat, ρ_l is the density of the melt, ε is the surface emissivity, σ_{SB} is the Stephan-Boltzman constant, T is the instantaneous temperature of the droplet, T_R the temperature of the gas (room temperature) and h_m the heat transfer coefficient of the droplet falling through a gas. The heat transfer coefficient, h_m, is given as:

$$h_m = \frac{\kappa^g}{d} \left(2.0 + 0.6 \sqrt{Re} \, \sqrt[3]{Pr} \right) \tag{3}$$

where κ^g is the thermal conductivity of the gas, Re the Reynolds number and Pr the Prandtl number, with the Reynolds and Prandtl numbers being given by:

$$Re = \frac{v^r \, \rho^g \, D}{\eta^g} \qquad\qquad Pr = \frac{C_p^g \, \eta^g}{\kappa^g} \tag{4}$$

where ρ^g is the density, η^g the dynamic viscosity, v^r flow velocity and C_p^g the specific heat of the back-fill gas.

The thermophysical constants used in the cooling rate calculation are given in Table 1.

Table 1: Thermophysical properties of N_2 and Al used in the cooling rate calculation.

Material	Parameter	Value
Nitrogen gas [25]	C_p^g	1039 (J kg^{-1} K)
	η^g	1.78 x 10^{-5} (N s m^{-2})
	κ^g	2.6 x 10^{-2} (W m^{-1} K^{-1})
	ρ^g	1.16 (kg m^{-3})
Aluminium [26]	C_p^l	1180 (J kg^{-1} K^{-1})
	C_p^s	910 (J kg^{-1} K^{-1})
	ρ_l	2385 (kg m^{-3})
	L	396 (kJ kg^{-1})

Figure 1 shows the calculated cooling rate of the solidifying droplets as a function of diameter, d. The cooling rate ranges between 150 K s^{-1} and 11,000 K s^{-1} for 850 µm and 53µm droplets,

respectively. Kasperovich *et al.* [27] and Erol *et al.* [23] have both estimated the cooling rates experienced during drop-tube processing. The estimated cooling rates here are lower than those in [23,27], due both to our use of N_2 as a cooling medium, which has a significantly lower thermal conductivity than He as used by Kasperovich *et al.* and Erol *et al.* and due to the lower liquidus temperature (and hence lower temperature differential between the melt and the ambient gas) of Al melts, compared to the melts studied by both Kasperovich *et al.* and Erol *et al.* Using a power law fit, the relationship between cooling rate, dT/dt, and droplet diameter, d, is written as:

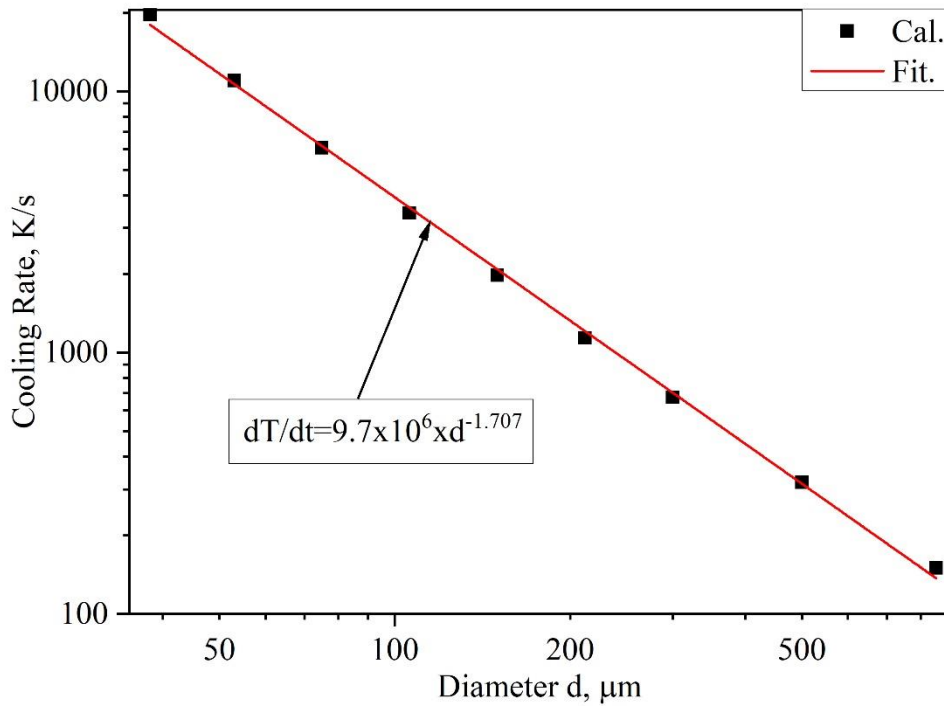$$\text{d}T/\text{d}t = 9.7 \text{ x } 10^6 \text{ x } (d/\mu\text{m})^{-1.707} \tag{5}$$

Figure 1: Estimated cooling rates of the droplets as a function of droplet size, *d*.

3.2 XRD Results

Figure 2 shows the XRD patterns of the rapidly solidified Al-2.85 wt% Fe as a function of droplet diameter. The XRD patterns indicate three intermetallics phases: equilibrium, monoclinic $Al_{13}Fe_4$, metastable, orthorhombic Al_6Fe and metastable, orthorhombic Al_5Fe_2. Al_5Fe_2 was probably formed at small volume fraction as it was not identified in the microstructure of the samples. α-Al, $Al_{13}Fe_4$ and Al_6Fe are the dominant phases for all sample sizes and, thus, cooling rates. With increasing cooling rate, in addition to these three phases, Al_5Fe_2 is observed in samples with a diameter smaller than 106 μm, with a corresponding cooling rate higher than 3300 K s^{-1}. It may be noted that, as the most intense diffraction peak of Al_5Fe_2 (311) overlaps with Al (200), it is difficult to distinguish these two peaks in XRD patterns.
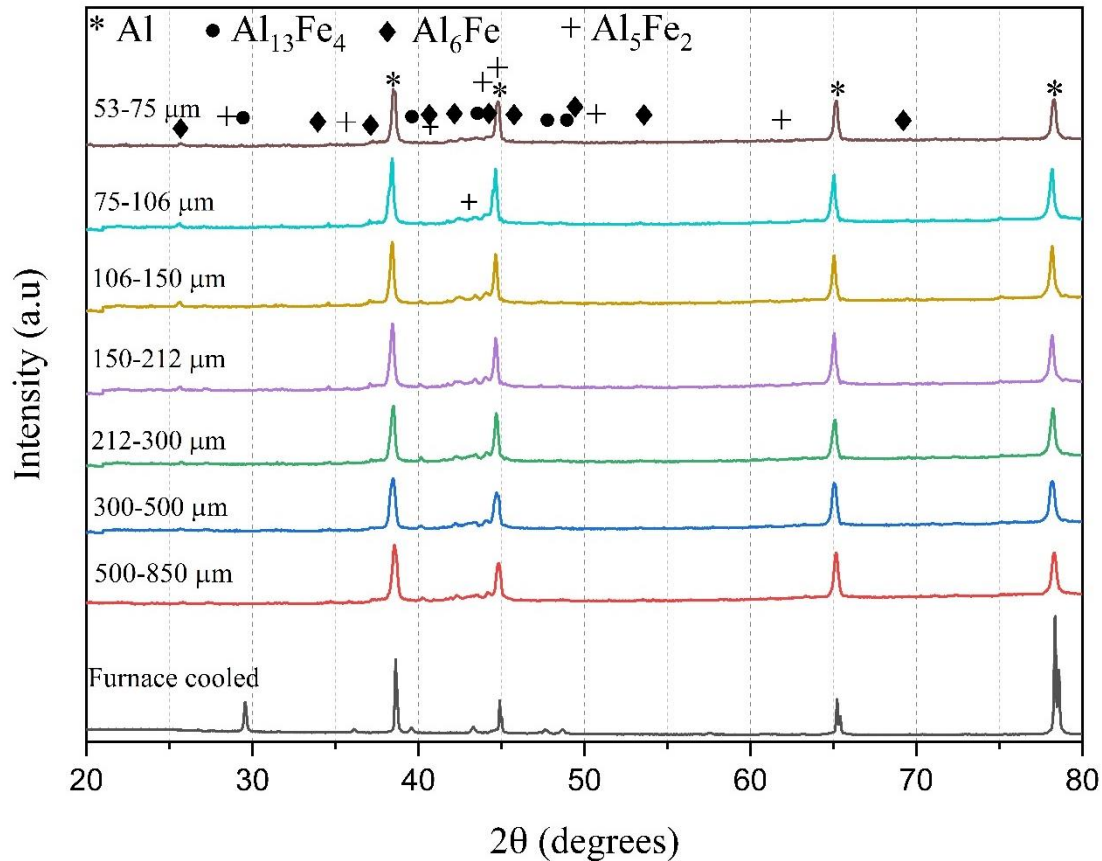
Figure 2: XRD patterns and phase identifications of the droplets as a function of size range.

3.3 Microstructure and phase identification

Figure 3 shows an SEM micrograph of the furnace cooled, Al-2.85 wt% Fe sample with an average cooling rate of 20 K min^{-1}. As the phase diagram of Al-Fe suggests, the microstructure consists of proeutectic $Al_{13}Fe_4$ and α-Al + $Al_{13}Fe_4$ eutectic. The proeuctectic $Al_{13}Fe_4$ has a compact, blocky morphology but this transitions into long thin needles radiating out from the initial blocky crystal during the eutectic growth phases. Note that, in the absence of primary α-Al, the growth of the intermetallic is unconstrained, leading to the observed thin needle like crystals of $Al_{13}Fe_4$. This is the classic morphology for this phase and the one which is attributed to causes such a significant drop in the mechanical properties of Fe-contaminated aluminium.
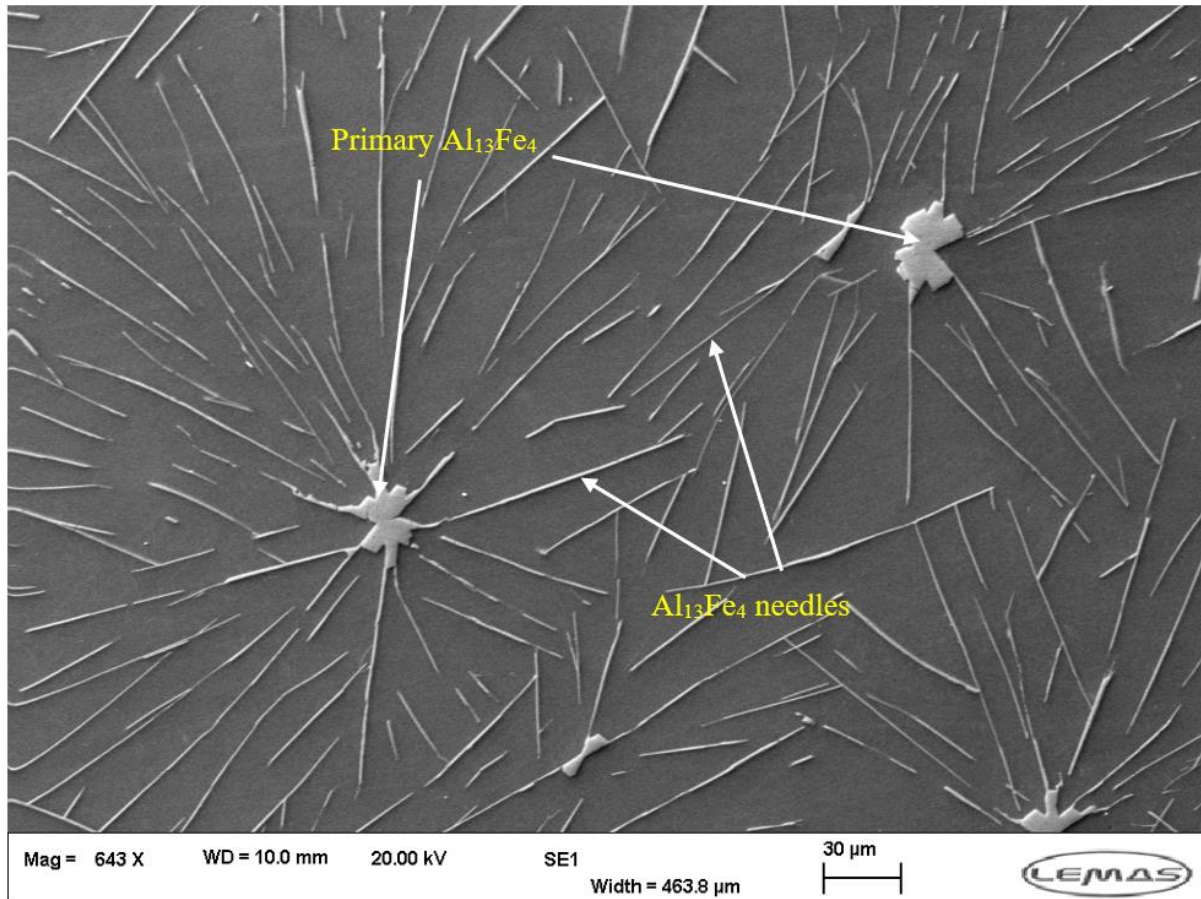
7

Figure 3: SEM micrograph of the drop tube cooled sample showing blocky $Al_{13}Fe_4$, $Al_{13}Fe_4$ needles and α-Al matrix.

Figures 4a and 4b show optical micrographs of the samples from the largest two size fractions, 850 µm < d < 500 µm and 500 µm < d < 300 µm, respectively. It is clear from the figure that there exist three distinctive regions: a microcellular region (designated with circles in the figures, which we hypothesise also indicate the location of nucleation on the sample), a dendritic region and a rod-like eutectic region. Magnified SEM images of these areas for a 850 µm < d < 500 µm droplet are given in Figure 5. From the extensive presence of dendrites, it can be seen that α-Al is the primary phase. According to the equilibrium phase diagram and the microstructure of the furnace cooled sample given in Figure 3, the primary phase expected is the $Al_{13}Fe_4$ intermetallic, the composition of the alloy being hypereutectic. However, it is evident from the microstructure (Figure 5 b and c)) that the primary phase formed is α-Al rather than $Al_{13}Fe_4$ intermetallic, which suggests that the resulting undercooled liquid was on the α-Al side of the eutectic coupled zone. This result accords with that made by [3], using impulse atomisation. The fine microcellular region, (figure 5a), consists of primary α-Al with a lamellar intercellular eutectic. This then transitions into a dendritic morphology for the α-Al, again with a lamellar interdendritic eutectic (Figure 5 b and c), followed by a transition to pure eutectic growth (Figure 5d), with this being a rod-like eutectic. According to [28], Al-Al_6Fe forms a fine rod-like morphology while Al-$Al_{13}Fe_4$ is a lamellar eutectic, wherein we tentatively associate this terminating eutectic as being that between α-Al and Al_6Fe, with the interdendritic lamellar morphology being that for the Al-$Al_{13}Fe_4$ eutectic (TEM-SAD confirmation of this is given in Section 3.3) Transitions in the solidification morphology, such as those observed here, are not

uncommon, particularly in eutectic melts [29], wherein the transition is usually associated with a drop in undercooling as solidification proceeds. As such, the fully eutectic microstructure is likely to represent the last portion of the droplet to solidify. As the Al_6Fe eutectic point (2.8 wt% Fe) is more iron rich than that for $Al_{13}Fe_4$ (1.8 wt% Fe), there appears to be no requirement for the growth of α-Al, the base alloy being very close in composition to the Al-Al_6Fe equilibrium eutectic. Thus, this marks a transition from interdendritic $Al_{13}Fe_4$ being the dominant intermetallic to rod-like Al_6Fe being the dominant form as distance away from the nucleation point increases. Using the ImageJ image processing software, the eutectic spacing of the intermetallics and fraction of α-Al were measured from Figure 5 and similar SEM micrographs. The average cross-sectional diameter of the rod-like Al_6Fe was measured as 140 nm and thickness of $Al_{13}Fe_4$ lamellar was measured as 120 nm. The fraction of the dendritic Al in Figure 5b is measured at 59 vol.%, while the interdendritic eutectic occupies 41 vol.%. Henein *et al*. [30] reported the average eutectic fraction for the impulse atomized Al-1.9 wt% Fe and Al-0.6 wt% Fe as 33.1 vol.% and 18.2 vol.%, respectively, with the higher volume fraction reported here likely reflecting the higher Fe content of these samples.
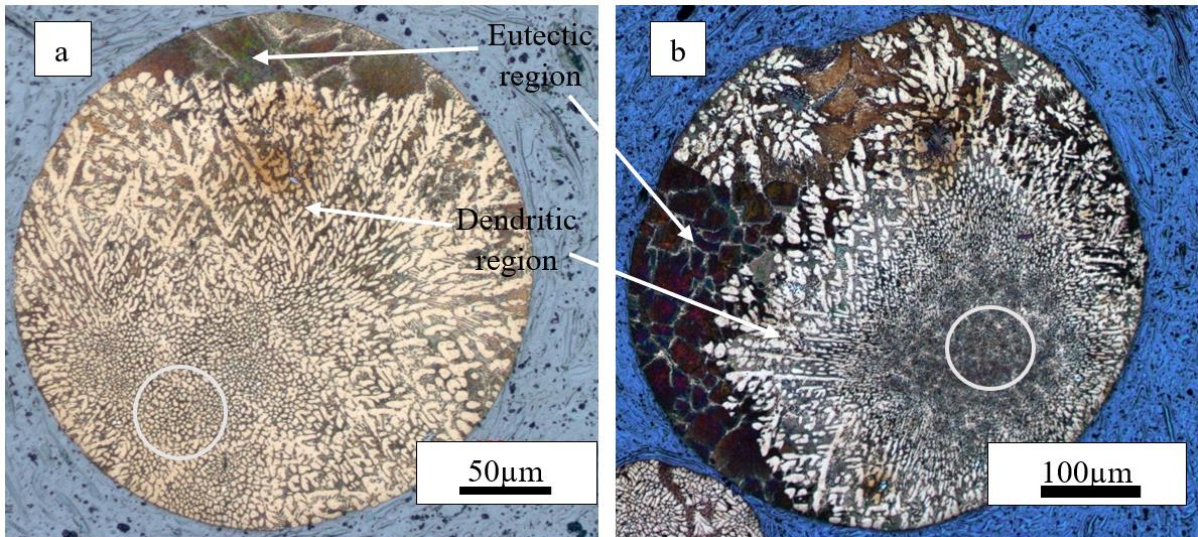

Figure 4: Microstructures of rapidly solidified Al-2.85 wt% Fe a) 850-500 µm and b) 500-300 µm droplets (circles showing the nucleation start zone).
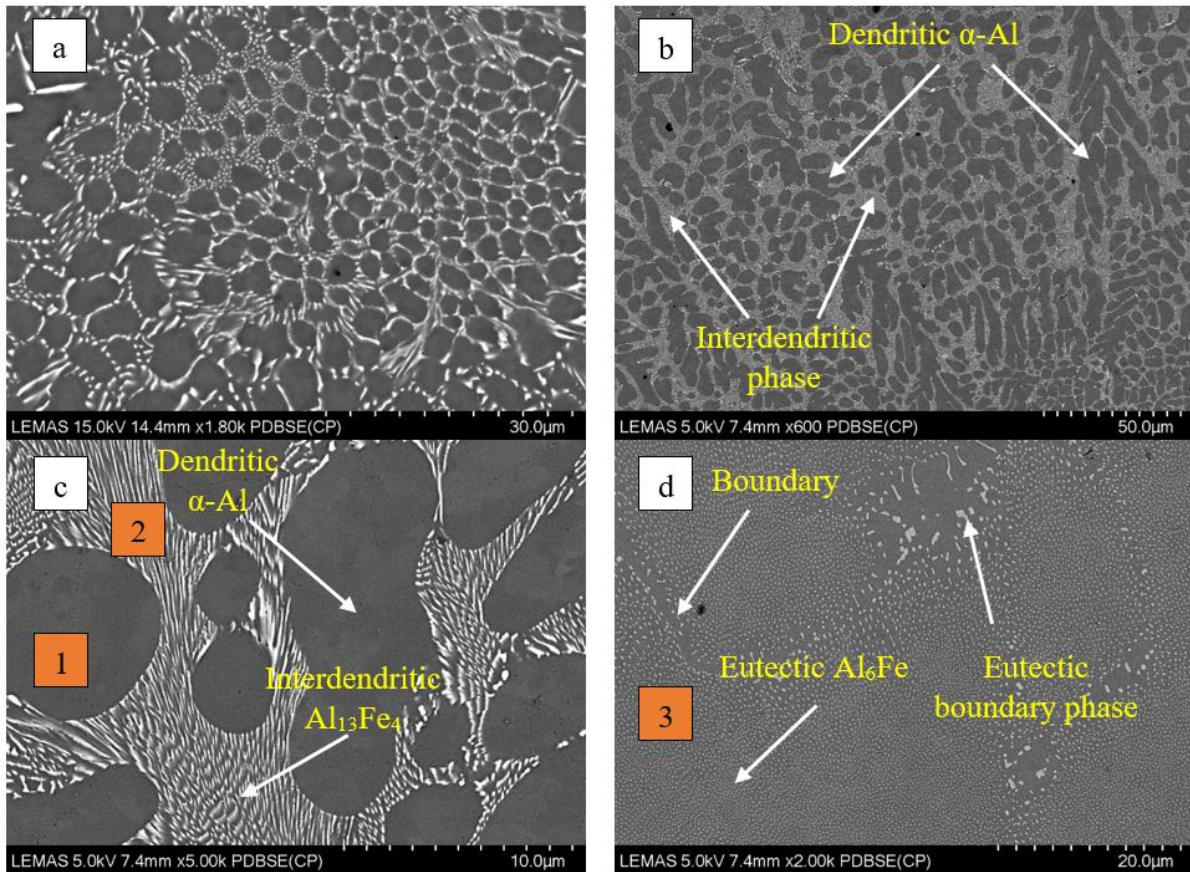
Figure 5: Typical microstructures of large droplets 850 µm< d < 500 showing a) magnified image of the nucleation region, microcellular region b) dendritic region, c) magnified image of the dendritic region and d) eutectic region.

Typical SEM microstructures for the 300 µm < d < 53 µm droplets are given in Figure 6. These droplets show dendritic and microcellular regions only. While some shows a single nucleation zone (designated with a circle), others appear to display multiple nucleation zones. Boundaries of the dendrites radiating from the nucleation zone(s) are indicated with arrows. There are two main changes in the microstructure compared to coarse droplets. Firstly, the fraction of α-Al in the dendritic portion of the microstructure rise as the droplet size decreases and correspondingly that of the eutectic phase decreases. This is likely due to the increasing cooling rate, and thus deeper undercooling, increases the permissible supersaturation of Fe in α-Al. This would permit a higher volume fraction of α-Al, and hence require less intermetallic. Secondly, below a droplet diameter of 300 µm we do not observe the pure α-Al + Al_6Fe eutectic as the terminating phase within the solidification sequence. Assuming that, in the largest droplet size fractions, this is due to a decrease in the undercooling towards the end of solidification, we would surmise that in the smaller size fractions the macroscopic heat extraction rate was sufficient to overcome this.
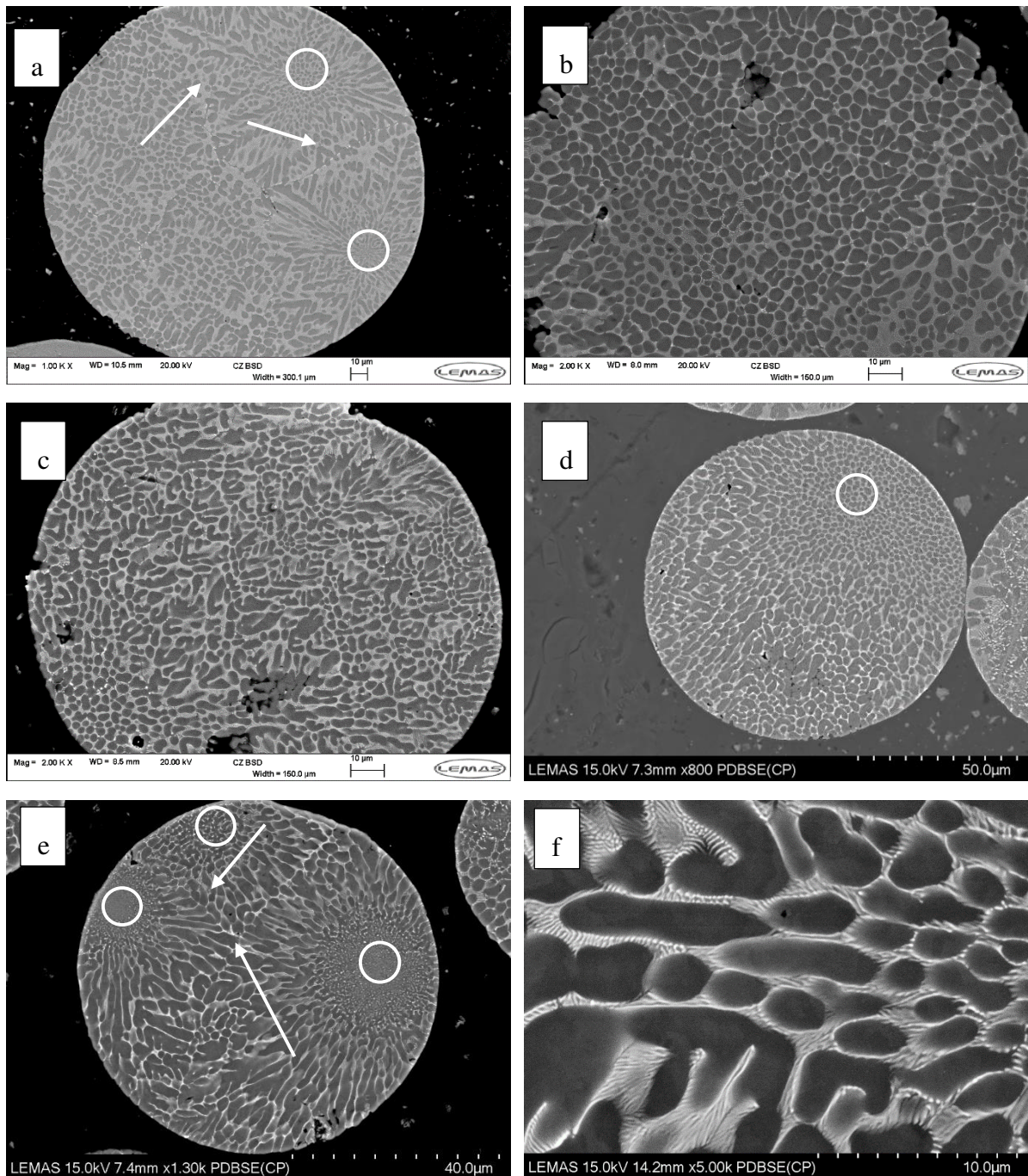
Figure 6: Microstructures of a) 300<d<212, b) 212<d<150, c) 150<d<106, d) 106<d<75 and e) 75<d<53 size fractions, with arrows showing boundaries of growing dendrites and circles showing the nucleation start zones. f) Enlarged view of the 106 < d < 75 µm sieve fraction showing that the interdendritic eutectic remains of the lamella morphology irrespective of sieve fraction/cooling rate.

The morphology of the microcellular region (presumed to be where solidification initiated) also changes with increasing cooling rate. The microstructures of the microcellular regions for the 106-75 and 75-53 µm spherical samples are given in Figure 7. Figure 7a shows microcellular structure 106-75 µm droplet where α-Al is surrounded by lamellar eutectic. This morphology is identical to the morphology of microcellular region of the 850-500 µm droplet given in Figure 5a, although somewhat finer. Figure 7b also shows the morphology of the

11

microcellular region in the 106-75 µm samples, but now a different eutectic morphology is evident. This we believe is a divorced eutectic, with this structure first being observed in this size fraction, which would therefore mark the transition from a fully lamellar eutectic to a mixed morphology containing both divorced and lamellar eutectic. The estimated average cooling rate for this transition is 4745 K s^{-1}, with similar structures being observed in the 75-53 µm samples, as shown in Figure 7c and 7d, with these samples experiencing higher cooling rates. Figure 7d illustrates this mixed morphology, showing the transition from the divorced to the lamellar eutectic as distance from the presumed nucleation point increases.
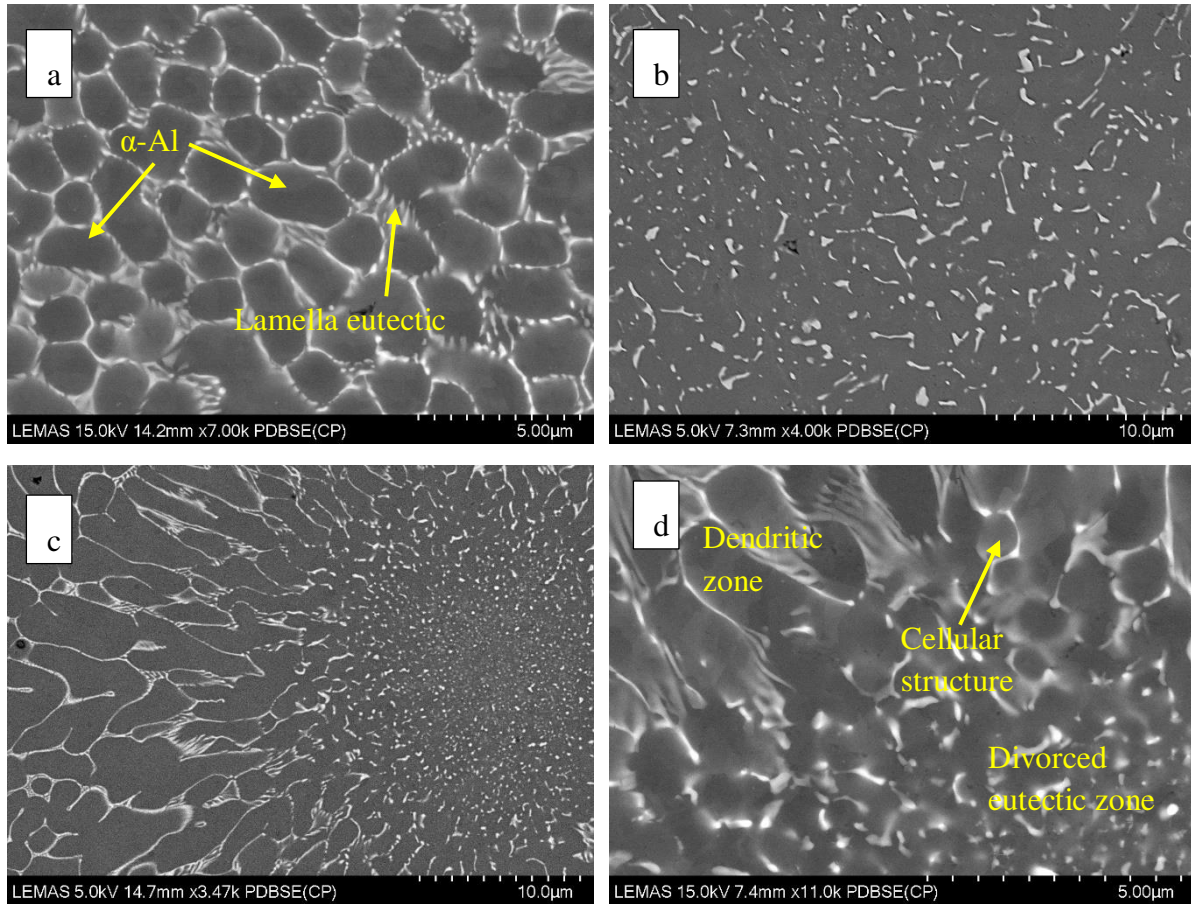

Figure 7: SEM BSE micrographs taken from the solidification start zone of a) 106-75 µm sample showing cellular α-Al surrounded by lamella-like eutectic, b) 106-75 µm sample showing divorced eutectic with intermetallics with various size and morphology, c) 75-53 µm sample depicting divorced eutectic on which dendritic α-Al grows with lamellar-like intermetallic and d) magnified image of solidification zone of c).

Secondary dendrite arm spacing

During drop tube processing it is not possible to monitor the thermal history of the droplets directly. Thus, there are two ways to estimate the cooling rates of the droplets: 1) using mathematical models and 2) using the secondary dendrite arm spacings of the samples. The estimated cooling rate of the droplets using a mathematical model was given in Figure 1. SDAS of the α-Al was measured for all sample sizes using image processing software. Figure 8 shows the measured SDAS for each sieve fraction, plotted as a function of the average cooling rate

12

for that sample size. This shows that the SDAS decreases with decreasing droplet size and, consequently, increasing cooling rate and ranges between 4.2 to 1.4 µm. Theoretically, it is predicted that [31] SDAS should scale as:

$$SDAS = K * \dot{T}^{-n} \tag{6}$$

where $\dot{T}$ is the cooling rate, K is a material constant and the exponent n ranges between 0.2 and 0.4. In this work, based upon cooling rates between 150 and 8000 K s^{-1} we calculate the parameters as being $K = 31.06$ and $n = 0.367$. The only other work of which we are aware in which these coefficients have been calculated for the Al-Fe system is that due to Miki *et al.* [32] who calculated K and n for an Al-0.55 wt% Fe alloy as 33.4 and 0.333, respectively, which are sufficiently close to the values determined here to give confidence in the cooling rate estimates used.
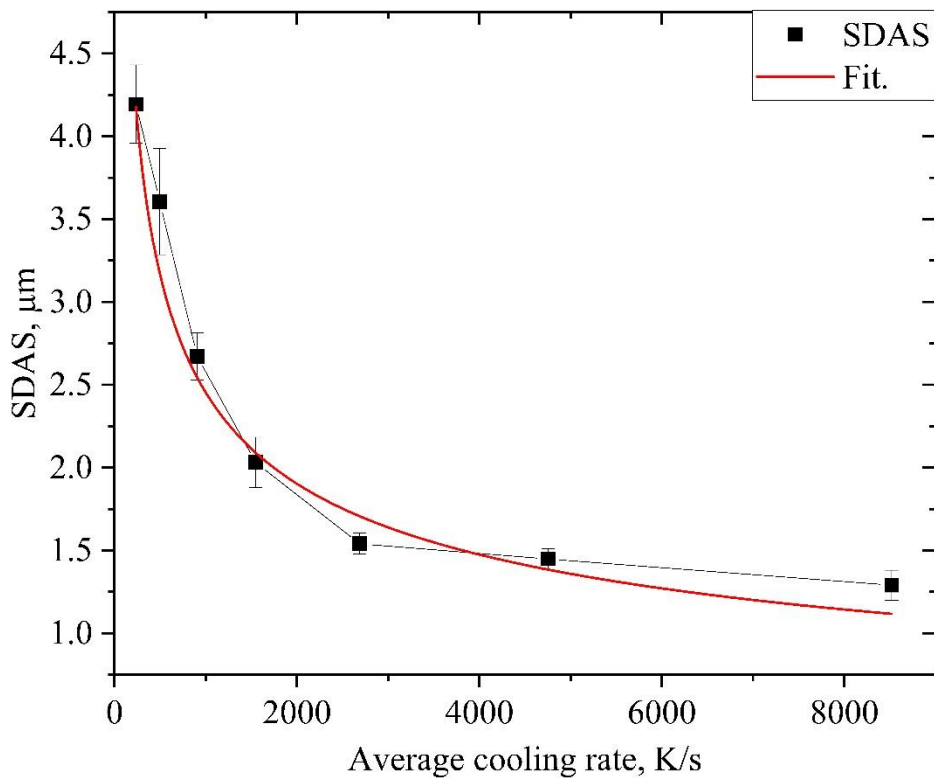

Figure 8: Secondary dendrite arm spacing (SDAS) as a function of average sample size.

EDS analysis

Using EDS analysis, the elemental composition of the primary α-Al, interdendritic eutectic and the terminating pure eutectic zones, as labelled in Figure 5, were measured as a function of the sample size in order to quantify the departure from equilibrium. As the intermetallics are very fine, it is not possible to get a representative EDS measurement from an individual intermetallic lamella, these being smaller than the interaction volume of the electron beam. Thus, instead of point EDS analysis, area EDS analysis was employed upon the eutectic regions.

Five to ten EDS measurements were taken from each sample size and the Fe content of α-Al as a function of average cooling rate is shown in Figure 9. The equilibrium Fe solubility in α-Al is limited, being around 0.05 wt. %Fe. However, rapid solidification resulted in the extension of the Fe solubility in α-Al. Fe solubility was found to rise to 0.37 wt. %Fe in the slowest cooled samples with an average corresponding cooling rate of 150 K s^{-1}. The solubility of Fe in α-Al rises with increasing cooling rate, tending more-or-less asymptotically to a limiting value of 1.105 wt% Fe at the highest cooling rates. Assuming that the Fe supersaturation may be uniquely related to the metastable extension of the α-Al solidus, the undercooling of the melt prior to nucleation may be estimated. Moreover, if the solidus line is linear with composition, this would correspond to undercoolings between 96 and 189 K, with the observed maximum supersaturation reflecting a maximum attainable undercooling for the material, with the likelihood being that further increases in cooling rate would lead to little or no further increase in supersaturation. Moreover, such a limiting value for the undercooling, which in turn will be determined be the efficacy of heterogeneous nucleation, will be highly sensitive to both the purity of the material used and the cleanliness of the processing conditions, potentially explaining why such a large range has previously been reported in the literature.

The elemental compositions of the interdendritic eutectic and eutectic zones were also measured. Regardless of the imposed cooling rate, the composition of the terminating eutectic zone did not change, with this being measured as 2.9 ± 0.2 wt. %Fe for sample sizes 850 μm < d < 500 μm and 500 μm < d < 300 μm (the terminating eutectic region only being observed in these two size fractions). To within experimental error, this figure corresponds to the Al-Al$_6$Fe eutectic composition (2.8 wt. %Fe), tending to confirm that the rod-like eutectic morphology is the α-Al + Al$_6$Fe eutectic and probably grew close to equilibrium. Moreover, by elimination, the lamellar morphology can be associated with the α-Al + Al$_{13}$Fe$_4$ eutectic. However, it is observed that the cooling rate does affected the composition of the interdendritic eutectic. Figure 10 shows the Fe content of the interdendritic eutectic as a function of average cooling rate. The lowest Fe content was measured as 3.9 wt% Fe in samples with size of 850-500 μm. This figure then rises with decreasing sample size, reaching a maximum of 4.8 wt. %Fe in the finest sample size. This would be consistent with a eutectic coupled zone that was skewed towards the intermetallic phase, wherein smaller droplets attaining higher undercoolings would be expected to show a more Fe-rich eutectic.
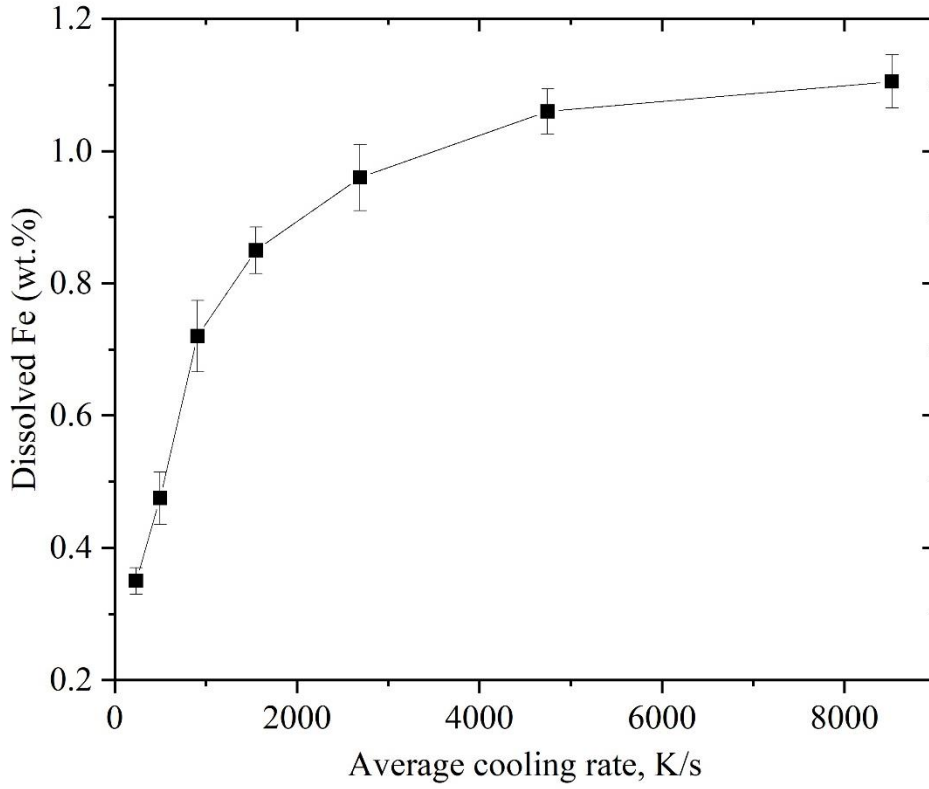
Figure 9: Dissolved Fe in α-Al as a function of average cooling rate.
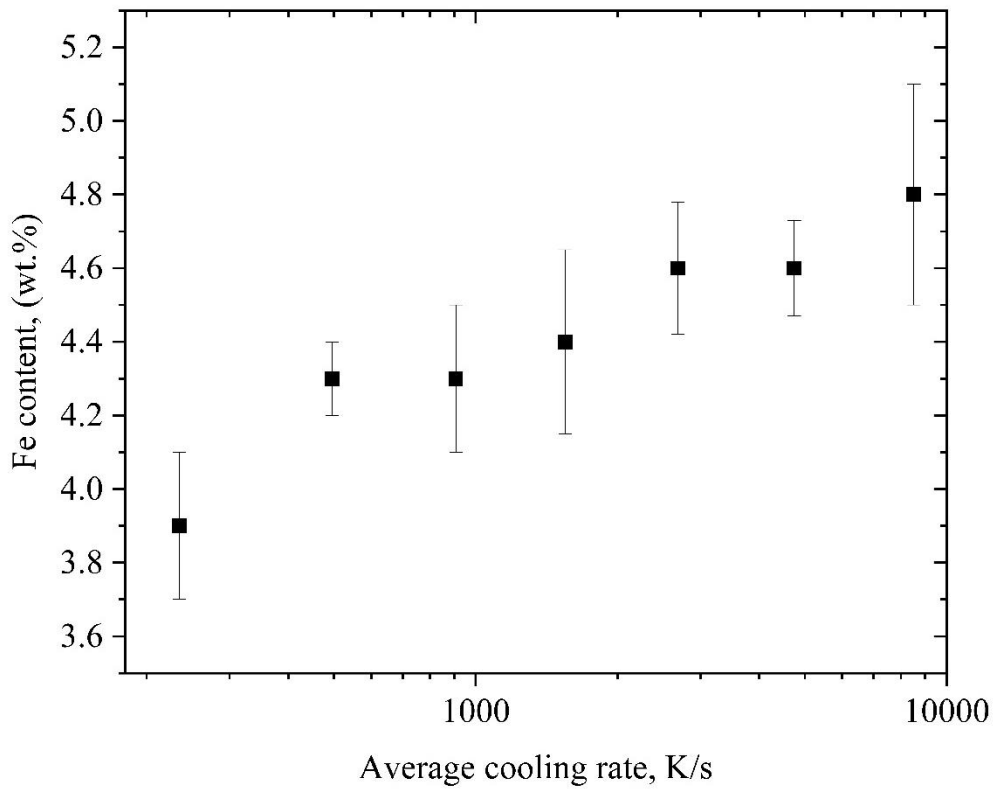

Figure 10: Composition of the interdendritic eutectic as a function of average cooling rate.

Eutectic volume fraction can be calculated from the SEM images by measuring the surface percent of the phase. Using image processing software, images were converted to grey scale format and a threshold function was employed to measure the fraction of the interdendritic eutectic. Figure 11 shows the interdendritic eutectic volume per cent as a function of average cooling rate. Boundaries of the corresponding cooling rate of the sieve fractions are given as error bars in the figure. It is clear from the figure that the trend is for the volume fraction of the interdendritic eutectic to decrease with increasing cooling rate. While the largest sample size fraction consisted of 49.5 vol. % interdendritic eutectic, this figure dropped to 26.7 vol. % in the smallest sample size. This is consistent with a higher Fe supersaturation in the α-Al and with the higher Fe content of the eutectic. As the cooling rate increases the eutectic growth rate may also be expected to increase and as a consequence the lamellar spacing should decrease. As shown in Figure 12 this is indeed the case, with the eutectic spacing ranging from 0.75 μm in the largest droplets to 0.15 μm in the smallest.
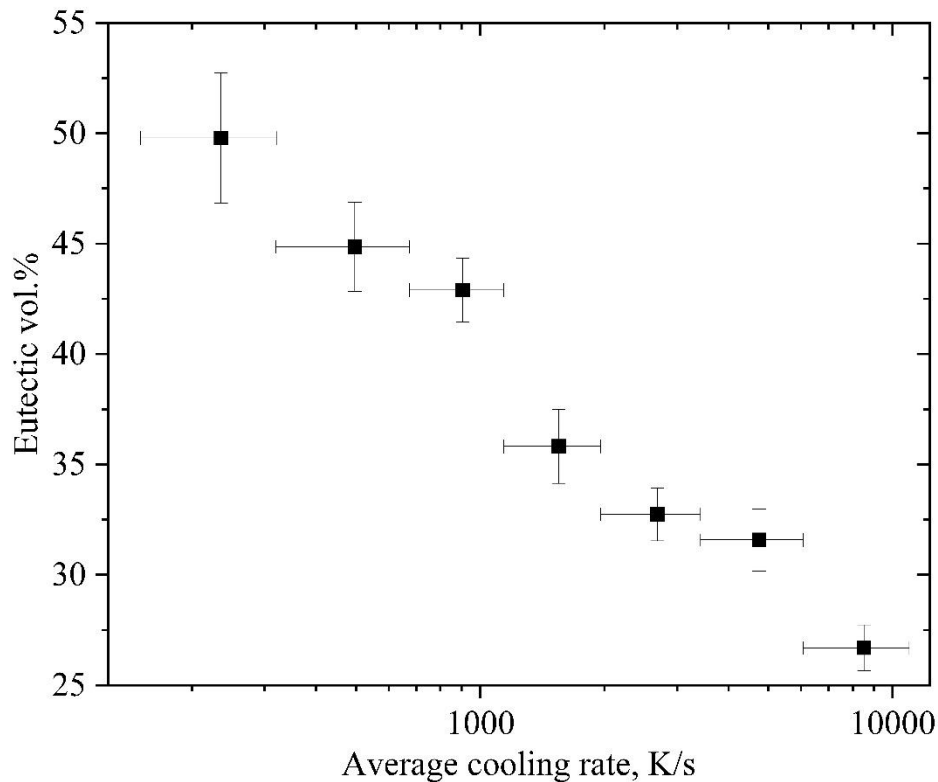

Figure 11: Eutectic volume per cent as a function of the average cooling rate.
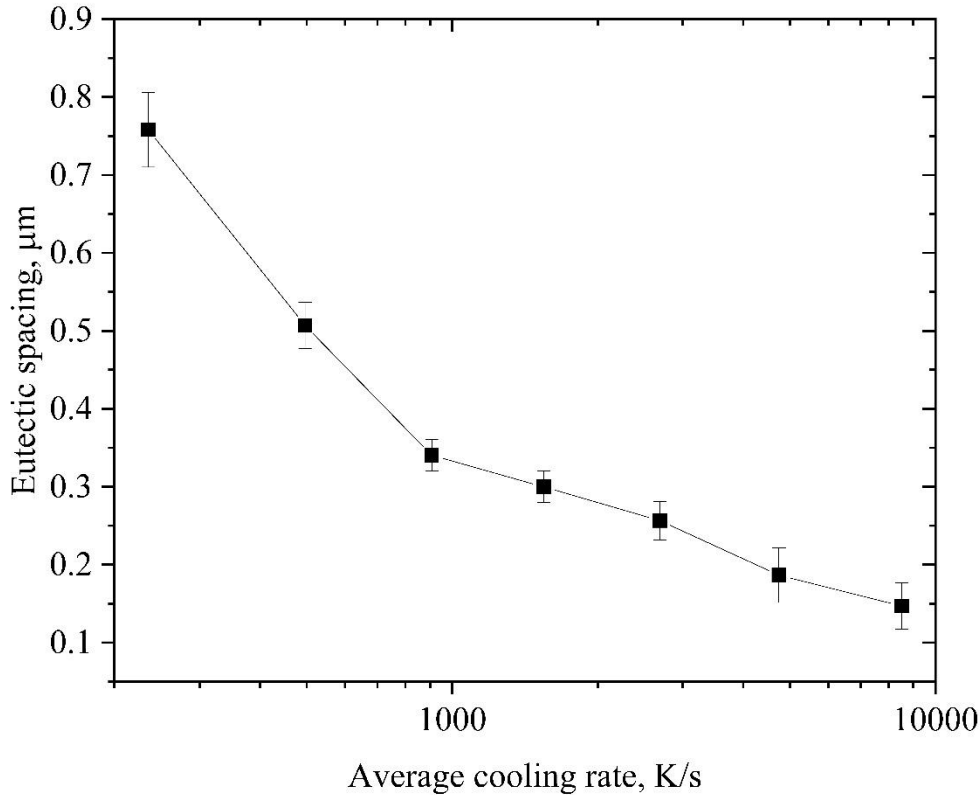
Figure 12: Interdendritic eutectic spacing as a function of average cooling rate.

TEM analysis

A FIB sectioned sample taken from the eutectic-interdendritic boundary region of 850-500μm sample was further examined under TEM. This region was selected as it contained both the pure rod-like eutectic phase and the interdendritic lamellar eutectic phase. Results are given in Figure 13. Figure 13a shows the TEM bright field image of the rod-like eutectic. A TEM Selected Area Diffraction (SAD) pattern (Figure 13b) taken along $[1\bar{1}0]$ zone axis from point 1 as labelled in Figure 13a, reveals this phase to be Al_6Fe. Figure 13c shows the TEM bright field image of lamellar eutectic. The TEM-SAD pattern given in Figure 13d reveals that the intermetallic phase in the lamellar eutectic is $Al_{13}Fe_4$. Moreover, in the transition region from interdendritic eutectic to rod-like eutectic there is a compact precipitate region, as shown in Figure 13e. The SAD pattern (Figure 13f) shows that this also belongs to $Al_{13}Fe_4$. Figure 13e also shows rod-like and acicular precipitates.

17

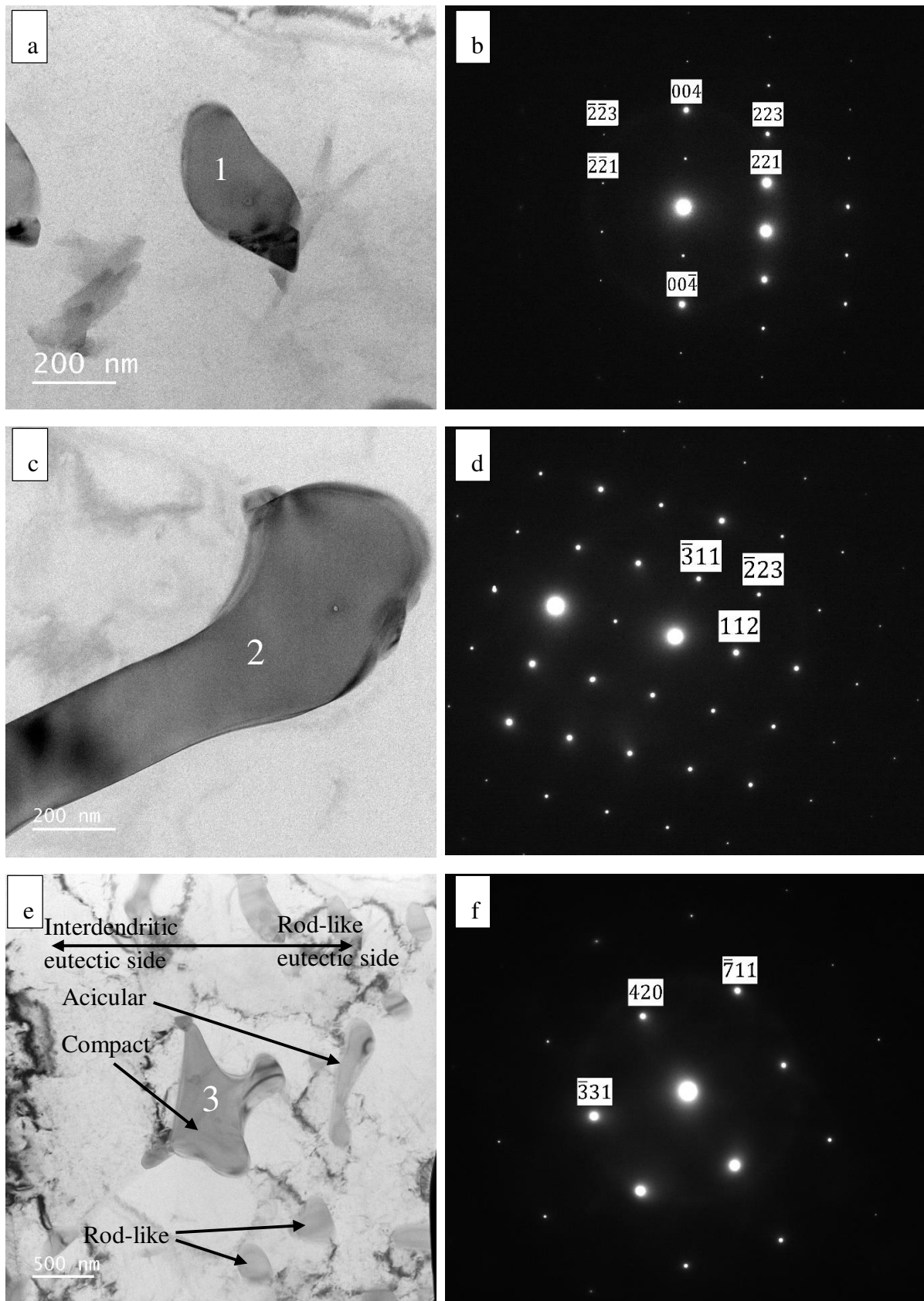Figure 13: a) TEM bright field image of the rod-like eutectic, b) TEM diffraction pattern of point 1 showing the diffraction pattern of Al_6Fe along the $[1\bar{1}0]$ zone axis, c) TEM bright field image of the lamella-like interdenritic eutectic, d) TEM diffraction pattern of point 2 depicting the diffraction pattern of $Al_{13}Fe_4$ along the $[\bar{1}\bar{7}4]$ zone axis, e)TEM bright field image of point

the intermetallic formed between rod-like eutectic and interdendritic eutectic, f) TEM diffraction pattern of point 3 depicting $Al_{13}Fe_4$ along the $[1\bar{2}3]$ zone axis.

3.4 Microhardness

In order to understand the effect of non-equilibrium solidification on the mechanical properties of the alloy, Vickers microhardness measurement have been employed on all sample fractions with a standard indenter using 10 g load and 10 s dwell time. The results are given in Figure 14. The minimum microhardness was observed in the slowest cooling droplet, 850 µm< d < 500, and measured as 53.5 ± 2 $HV_{0.01}$. Microhardness values of the droplet then gradually rise with increasing cooling rate and reached a maximum value of 66.14 ± 1.14 $HV_{0.01}$ in the 106 µm < d < 75 µm droplets. The total increase in the microhardness is however limited, being only around 20%. This relatively small increase in microhardness, despite the large departures from equilibrium experienced during solidification, is likely to be due to the competition between increasing superaturation and scale refinement [33] with increasing cooling rate, both of which will tend to increase the microhardness and a decreasing volume fraction of intermetallic, which will tend to oppose the increasing microhardness.
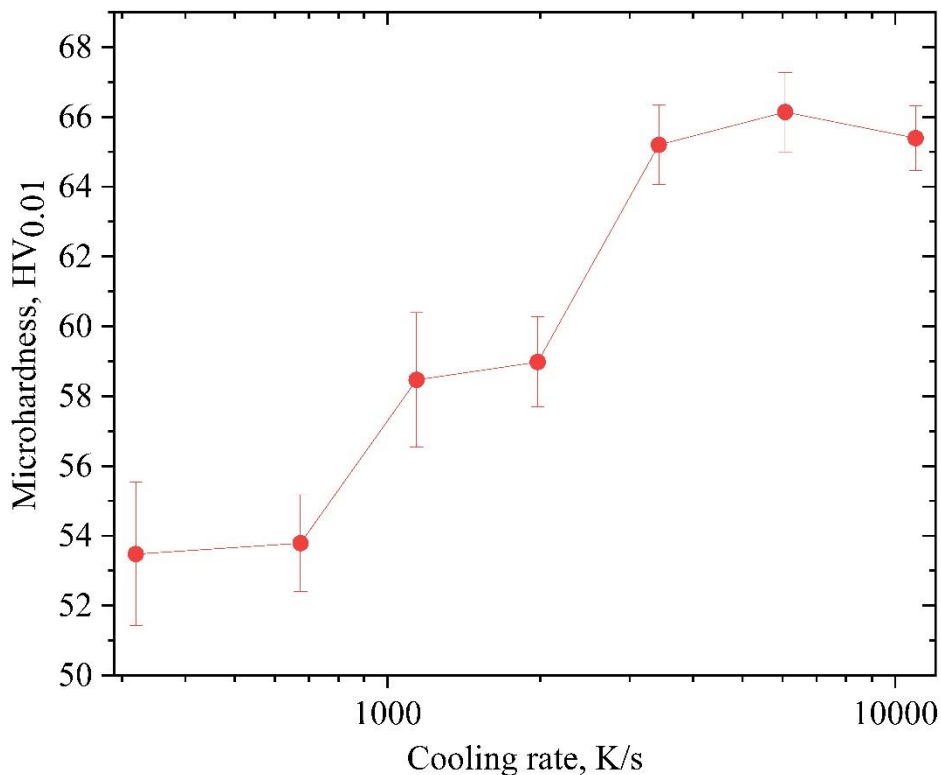

Figure 14: Microhardness value (in $HV_{0.01}$) as a function of cooling rate.

4. Discussion

An Al-2.85 wt% Fe alloy has been subjected to nonequilibrium solidification using drop tube processing, with cooling rates ranging between 150 and 11000 K s^{-1}. An increase in Fe

solubility in the α-Al phase is observed with increasing cooling rate, with this ranging from 0.37 wt% Fe at the lowest cooling rate to 1.105 wt% Fe at the highest cooling rate. For commercial secondary or mixed alloy Al scrap, this would mean that even with fairly high Fe contents, techniques such as gas atomization, which produce cooling rates similar to those discussed here [34], should be able to produce Al powders free from intermetallics. This contradicts to the finding of Nayak *et al.* [4], who observed that the dissolved Fe content decreases with increasing wheel speed, and consequently increasing cooling rate, in melt-spun Al-Fe alloys. Due to the higher supersaturation of Fe retained in solid solution at these higher cooling rates, it is expected that the interdendritic eutectic volume fraction should decrease with increasing cooling rate. As shown in Figures 8 and 10, eutectic volume fraction and Fe solubility in α-Al are indeed inversely related.

However, if intermetallics do form, control of the phases formed does not appear to be easily possible. In particular, SEM analysis suggests that increasing the cooling rate does not shift the interdendritic eutectic from that based on $Al_{13}Fe_4$ to that based on Al_6Fe. On the contrary, while intermediate cooling rate gives a mixed eutectic, increasing the cooling rate tends to promote the formation of just $Al_{13}Fe_4$. For the Al-$Al_{13}Fe_4$ eutectic, the relationships between λ, v and ΔT have been well characterised [16,35] so that we may write $\lambda \sqrt{v} = 22.4 \ \mu m^{1.5} s^{-0.5}$ and $\lambda \Delta T = 8.79 \ \mu m \ K$, wherein the measured lamellar spacing given in Figure 12 may be converted to an estimate of the growth rate for the interdendritic eutectic and the undercooling at the eutectic front. This conversion is shown in Figure 15.
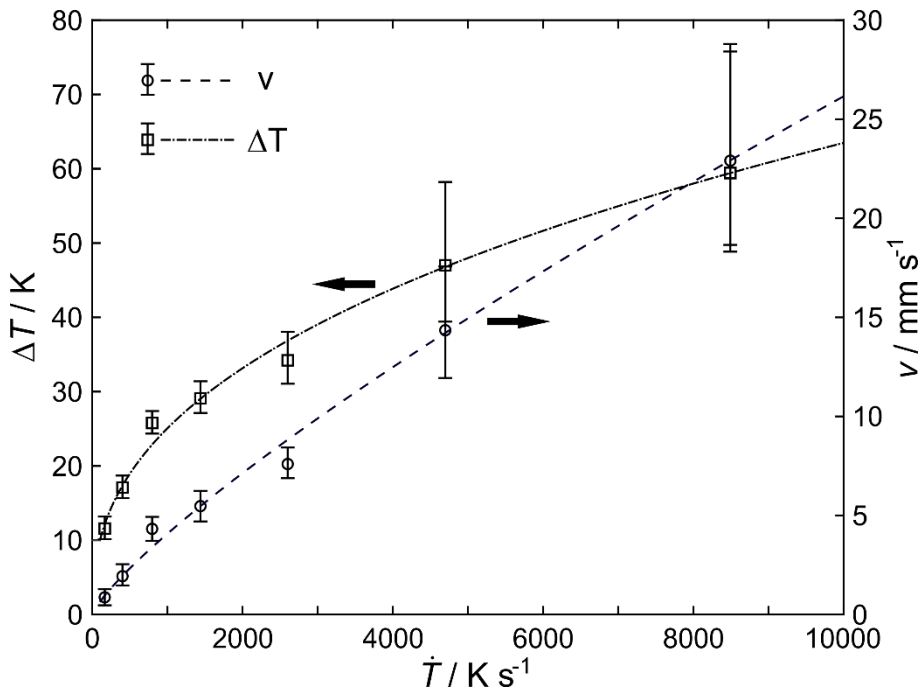

Figure 15: Eutectic growth velocity (right-hand axis) and interfacial undercooling (left-hand axis) for the Al-$Al_{13}Fe_4$ lamellar eutectic, estimate from the lamellar spacing.

What is striking in Figure 15 is the high growth velocities and the commensurately high interface undercoolings observed here for the growth of the Al-$Al_{13}Fe_4$ lamellar eutectic. This finding is both novel and contrary to the body of literature on phase selection in Al-Fe alloys conducted via Bridgman growth. Typically, in such Bridgman studies $Al_{13}Fe_4$ begins to be

replaced by Al_6Fe at growth velocities of around 0.1 mm s^{-1}, with the transition being complete between 1-10 mm s^{-1} (depending upon Fe concentration), with the maximum interface undercooling being no more than a few Kelvin [28]. Conversely, here we observe the Al-$Al_{13}Fe_4$ eutectic at growth velocities in excess of 20 mm s^{-1}, with a corresponding interfacial undercooling of nearly 60 K. We tentatively suggest that this difference reflects a fundamental difference in the phase selection behaviour of Al-Fe alloys depending upon whether growth is in a positive temperature gradient (Bridgman growth) or a negative temperature gradient (deeply undercooled droplets). In particular, the easier nucleation of $Al_{13}Fe_4$ in deeply undercooled melts (relative to Al_6Fe), may be a possible mechanism contributing to this effect.

Most of the droplets considered in this study appear to show just a single nucleation event, particularly in the larger size fractions, although this is not universally so. Figure 6b shows a droplet displaying multiple nucleation sites (3 nucleation sites shown with white circles) on which primary dendrites grow. Multiple nucleation sites can occur when there are a) multiple homogeneous nucleation sites, b) multiple impurities in the melt or c) dendrites breaking and providing sites for multiple nucleation, with both (b) and (c) representing heterogenous nucleation. We consider it unlikely, given the estimated undercoolings for these droplets, that homogeneous nucleation is able to occur. Similarly, as the cooling rates for the droplets in Figure 6 a and e are fairly high, there is likely to be insufficient time for dendrite fragments to be swept into the melt. Moreover, flow velocities in the drop-tube processed samples are likely to be very low, and thus it is unlikely that dendrite fragmentation is the reason for the multiple nucleation. Consequently, it is likely that at least some droplets are experiencing multiple heterogeneous nucleation events, either on impurities or surface oxides. Such multiple nucleation events become more likely as the undercooling increases, as the nucleation energy barrier decreases as $1/(\Delta T)^2$. Moreover, if such multiple surface nucleation events result in the last liquid to solidify being towards the centre of the droplet, rather than on its margins, the probability of mixed microstructures being observed in small size fractions will be increased. This would be in line with studies that show that gas atomised powders can show significant variability, even within a given size fraction, due to the stochastic nature of nucleation and the considerable consequent variability in the nucleation undercooling [36].

The Fe content of the interdendritic eutectic (Figure 10) was found to increase with increasing cooling rate, which would be consistent, as mentioned above, with a eutectic coupled zone being skewed towards the intermetallic. In fact, as both the composition and the undercooling (and hence interfacial temperature) of the eutectic are known, the left-hand (Al-rich) side of the coupled zone may be reconstructed, with the data points from Figures 10 and 15 being shown in Figure 16, superimposed upon the metastable phase diagram. What is surprising here is that the boundary of the coupled zone is displaced so far from the equilibrium eutectic point, although given the consistency of the EDS composition measurements made on the eutectic, we consider that this result is likely to be reliable. Also shown on Figure 16 is, for one size fraction (150-106 μm), the conjectured solidification path. The droplet undercooling, estimated from the supersaturation of the α-Al phase is 93 K, wherein primary solidification yields a volume fraction of around 67.5 vol.% α-Al with an Fe content of 0.95 wt%. Termination of primary α-Al growth occurs at an undercooling of 34 K, transitioning to an Al-$Al_{13}Fe_4$ eutectic

with an average Fe concentration of 4.6 wt% Fe, this comprising the remaining 32.5 vol.% of the microstructure.

In summary, we conclude that rapid solidification via powder metallurgical techniques are likely to provide a useful upcycling route for mixed Al scrap that is not too heavily contaminated with tramp Fe, as fairly substantial increases in the solid solubility of Fe mean that this can be retained in solid solution at cooling rates appropriate to such processes. Moreover, a number of researchers have shown that the mechanical properties of rapidly solidified Al-Fe alloys can further be improved by heat treatment, with this resulting in the formation of very fine spherical and needle-like precipitates, which can easily be controlled depending on the dwell temperature and time. However, for more heavily Fe contaminated scrap, such powder metallurgical processing appears to offer little control over the phase selection of the intermetallics present, with Al-Al$_{13}$Fe$_4$ being the dominant intermetallic observed at all cooling rates. However, scale refinement of the intermetallic may render it somewhat less harmful to mechanical properties, particularly in smaller powder sizes.
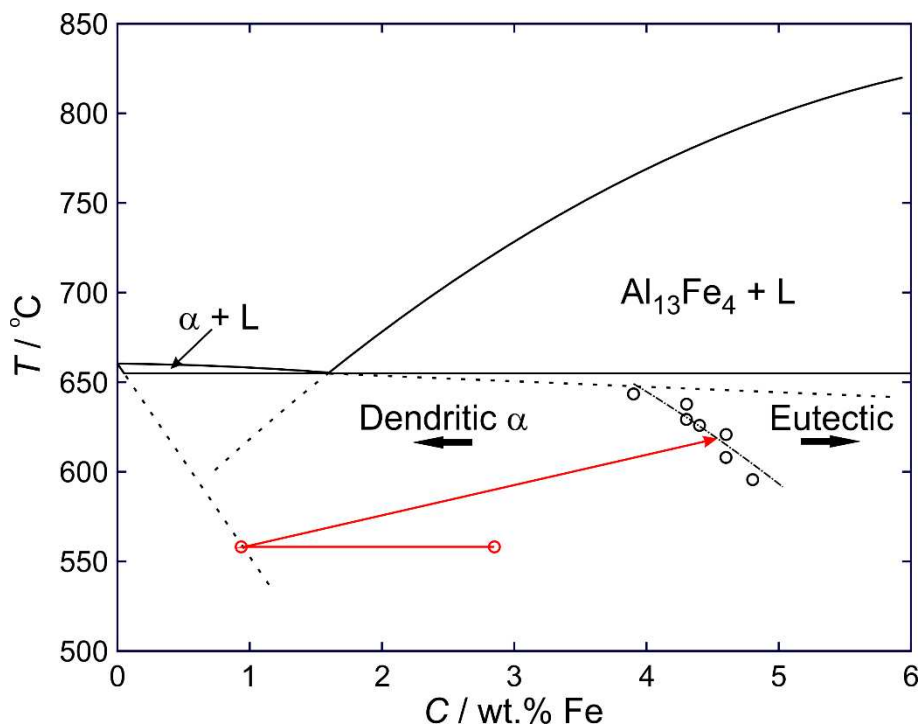

Figure 16: Estimated location of the Al-rich side of the eutectic coupled zone for the growth of Al-Al$_{13}$Fe$_4$ eutectic.

5. Conclusions

In the present work, rapid solidification of Al-2.85 wt.% Fe droplets within the diameter range of 850-53 µm with estimated cooling rates ranging between 155-11500 K s^{-1} were produced under containerless condition using a 6.5 m drop tube. The results are summarized as follows.

1) Microstructure of the large samples consisted of dendritic α-Al, lamellar eutectic and rod-like eutectic. Rod-like eutectic disappeared with decreasing sample size.
2) Dissolved Fe in α-Al was found to be increasing with decreasing sample size (increasing cooling rate) from 0.35 wt.% Fe to 1.105 wt.% Fe.

22

3) TEM results revealed that lamellar eutectic is Al-$Al_{13}Fe_4$ while rod-like eutectic is Al-Al_6Fe.

4) Al-$Al_{13}Fe_4$ eutectic was observed at growth velocities in excess of 20 mm s^{-1}.

5) Microhardness was found to be increasing from 53.5 ± 2 $HV_{0.01}$ to 66.14 ± 1.14 $HV_{0.01}$ with increasing cooling rate.

6. References

1. Liu W, Yang J, Xiao B. Application of Bayer red mud for iron recovery and building material production from alumosilicate residues. J Hazard Mater. 2009;161(1):474–8.

2. Zhang L, Gao J, Damoah LNW, Robertson DG. Removal of iron from aluminum: A review. Miner Process Extr Metall Rev. 2012;33(2):99–157.

3. Chen J, Dahlborg U, Bao CM, Calvo-Dahlborg M, Henein H. Microstructure evolution of atomized Al-0.61 wt pct Fe and Al-1.90 wt pct Fe alloys. Metall Mater Trans B Process Metall Mater Process Sci. 2011;42(3):557–67.

4. Nayak SS, Chang HJ, Kim DH, Pabi SK, Murty BS. Formation of metastable phases and nanocomposite structures in rapidly solidified Al-Fe alloys. Mater Sci Eng A. 2011;528(18):5967–73.

5. Kim DH, Kim SH, Kim NJ. Structure and decomposition behavior of rapidly solidified Mg-Al-Zn-Nd. TMS Annu Meet. 1995;29:435–47.

6. Sasaki TT, Ohkubo T, Hono K. Microstructure and mechanical properties of bulk nanocrystalline Al-Fe alloy processed by mechanical alloying and spark plasma sintering. Acta Mater [Internet]. 2009;57(12):3529–38. Available from: http://dx.doi.org/10.1016/j.actamat.2009.04.012

7. Murray JL. Alloy Phase Diagrams, Ed. by LH Bennett, TB Massalski and BC Giessen. In: Material Research Society Symposia Proceedings, Elsevier Science Publishing. 1983. p. 249.

8. Hughes IR, Jones H. Coupled eutectic growth in Al-Fe alloys. J Mater Sci. 1976;11(10):1781–93.

9. Hughes IR, Jones H. Coupled eutectic growth in Al-Fe alloys. J Mater Sci. 1977;12(2):323–33.

10. Mukhopadhyay DK, Suryanarayana C, Froes FH. Structural evolution in mechanically alloyed Al-Fe powders. TMS Annu Meet. 1995;26(AUGUST):191–202.

11. Nayak SS, Murty BS, Pabi SK. Structure of nanocomposites of Al-Fe alloys prepared by mechanical alloying and rapid solidification processing. Bull Mater Sci. 2008;31(3):449–54.

12. Çadırlı E, Herlach DM, Volkmann T. Characterization of rapidly solidified Ni–Si and Co–Al eutectic alloys in drop tube. J Non Cryst Solids. 2010;356(9–10):461–6.

13. Çadırlı E. Investigation of the microhardness and the electrical resistivity of undercooled Ni–10 at.% Si alloys. J Non Cryst Solids. 2011;357(3):809–13.

14. Cotton JD, Kaufman MJ. Microstructural evolution in rapidly solidified Al-Fe alloys: An alternative explanation. Metall Trans A. 1991;22(4):927–34.

15. Olsen KP, Sterzik G, Henein H. Microstructural refinement in Al alloys by impulse atomization. Int J powder Metall. 2001;37(1):55–64.

16. Lü P, Wang HP. Observation of the transition from primary dendrites to coupled growth induced by undercooling within Ni[sbnd]Zr hyperperitectic alloy. Scr Mater. 2017;137:31–5.

17. Li S, Wu P, Fukuda H, Ando T. Simulation of the solidification of gas-atomized Sn-5mass%Pb droplets. Mater Sci Eng A. 2009;499(1–2):396–403.

18. Mullis AM, Bigg TD, Adkins NJ. Structure and phase-composition of Ti-doped gas atomized Raney-type Ni catalyst precursor alloys. Intermetallics [Internet]. 2015;67:63–8. Available from: http://dx.doi.org/10.1016/j.intermet.2015.07.016

19. Tonejc A. X-ray study of the decomposition of metastable Al-rich Al-Fe solid solutions. Metall Trans. 1971;2(2):437–40.

20. Belov NA, Aksenov AA, Eskin DG. Iron in aluminium alloys: impurity and alloying element. CRC Press; 2002.

21. Cochrane RF, Evans P V., Greer AL. Containerless solidification of alloys in a drop-tube. Mater Sci Eng. 1988;98(C):99–103.

22. Sharma SC, Volkmann T, Herlach DM. Microstructural development in drop-tube-solidified Al-3.6wt.%Fe droplets: an analysis. Mater Sci Eng A. 1993;171(1–2):169–73.

23. Erol M, Büyük U. Solidification Behavior of Ge–Al Eutectic Alloy in a Drop Tube. Trans Indian Inst Met. 2016;69(4):961–70.

24. Oloyede O, Bigg TD, Cochrane RF, Mullis AM. Microstructure evolution and mechanical properties of drop-tube processed, rapidly solidified grey cast iron. Mater Sci Eng A. 2016;654:143–50.

25. Lee ES, Ahn S. Solidification progress and heat transfer analysis of gas-atomized alloy droplets during spray forming. Acta Metall Mater. 1994;42(9):3231–43.

26. Chu MG, Granger DA. Solidification and microstructure analysis of rapidly solidified melt-spun Al-Fe alloys. Metall Trans A. 1990;21(1):205–12.

27. Kasperovich G, Volkmann T, Ratke L, Herlach D. Microsegregation during solidification of an Al-Cu binary alloy at largely different cooling rates (0.01 to 20,000 K/s): Modeling and experimental study. Metall Mater Trans A Phys Metall Mater Sci. 2008;39 A(5):1183–91.

28. Wang Y, Jones H, Evans P V. Eutectic solidification characteristics of Bridgman grown Al-3Fe-0.1V alloy. J Mater Sci. 1998;33(21):5205–20.

29. Mullis AM, Clopet CR. On the origin of anomalous eutectic growth from undercooled melts: Why re-melting is not a plausible explanation. Acta Mater. 2018;145:186–95.

30. Henein H, Buchoud V, Schmidt RR, Watt C, Malakhor D, Gandin CA, et al. Droplet solidification of impulse atomized Al-0.61Fe and Al-1.9Fe. Can Metall Q. 2010;49(3):275–92.

31. Jones H. On the prediction of lattice parameter vs. concentration for solid solutions extended by rapid quenching from the melt. Scr Metall. 1983;17(1):97–100.

32. Miki I, Kosuge H, Nagahama K. Supersaturation and decomposition of Al-Fe alloys during solidification. J Japan Inst Light Met. 1975;25(1):1–9.

33. Ruan Y, Wang XJ, Chang S-Y. Two hardening mechanisms in high-level undercooled Al–Cu–Ge alloys. Acta Mater. 2015;91:183–91.

34. Mullis AM, Farrell L, Cochrane RF, Adkins NJ. Estimation of cooling rates during close-coupled gas atomization using secondary dendrite arm spacing measurement. Metall Mater Trans B. 2013;44(4):992–9.

35. Liang D, Jones H. The effect of growth velocity on growth temperature of the Al-Al3Fe and Al-Al6Fe eutectics. Zeitschrift für Met. 1992;83(4):224–6.

36. Mullis AM, Bigg TD, Adkins NJ. A microstructural investigation of gas atomized Raney type Al-27.5 at.% Ni catalyst precursor alloys. J Alloys Compd. 2015;648:139–48.

Acknowledgments